An Isolated Bidirectional Microinverter Based on Voltage-in-Phase PWM-Controlled Resonant Converter

Hongfei Wu, *Senior Member, IEEE*, Xinxi Tang, Jian Zhao, and Yan Xing, *Member, IEEE*

***Abstract*—A single-stage single-phase isolated bidirectional microinverter based on a voltage-in-phase pulsewidth modulation (VIP-PWM)-controlled resonant converter is proposed in this article. With the VIP-PWM control, the voltage conversion ratio of the resonant converter can be regulated from zero to infinity, theoretically, which means the VIP-PWM is suitable for wide-voltage-range applications, such as single-stage isolated inverters. Moreover, the voltage conversion ratio of the resonant converter is only determined by the equivalent duty cycle and is independent of the value and the direction of the transferred power. Therefore, the value and the direction of the power flow can be changed smoothly, which makes the proposed converter suitable for bidirectional dc–ac power conversion. Accordingly, a simple unified current controller can be employed for both inverter and rectifier modes. In addition, soft switching can be achieved during most of the grid period, and high efficiency can be achieved with the proposed solution. Detailed operation principles, characteristics, design considerations, and control strategy of the proposed microinverter are presented. A 300-W prototype with an input voltage range of 25–40 V is established and tested to verify the effectiveness and feasibility of the proposed solution.**

***Index Terms*—Bidirectional microinverter, energy storage applications, resonant converter, soft-switching, voltage-in-phase pulsewidth modulation (VIP-PWM).**

I. Introduction

OWING to the accelerating energy shortage and the exhaustion of global resources, renewable energies, such as photovoltaic (PV) and electric vehicles (EVs), have been receiving increasing interest, especially in the residential area [1], [2]. However, the conflict between production and consumption of solar energy is a fundamental problem for homeowners: energy consumption is the highest in the morning and evening, while solar production peaks during midday. Fig. 1 illustrates a typical residential PV system with a battery and an EV. The surplus solar energy is consumed by batteries to mitigate the influence of excess solar energy. When needed, the energy stored in the batteries will be released to supply the load. If necessary, the EV car can also help power the load. The bidirectional grid-connected dc–ac converter is the key to achieve energy management.

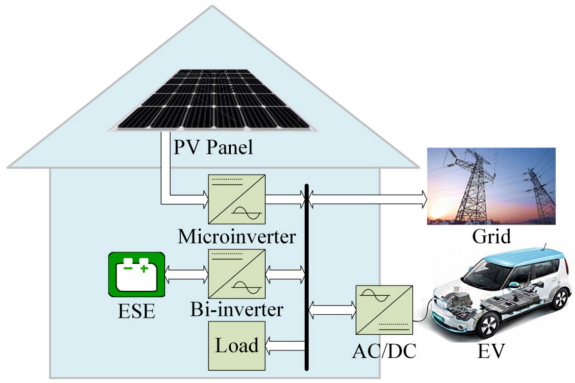

Fig. 1. Typical structures of residential power systems.

For grid-connected applications, galvanic isolation is a basic requirement for safety considerations. Isolated dc–ac converters can be categorized into two groups: two-stage and single-stage converters [3], [4]. Compared with two-stage solutions, a single-stage solution can directly convert dc to line-frequency ac with only one-stage conversion, resulting in reduced number of power switches, higher efficiency, and minimized high dc voltage indoors. Since the parasitic resistance of the battery at low frequency is very small, the double-line-frequency ripple is induced in the charging current with the single-stage solutions. Many research studies have been conducted on the impact of double-line-frequency current ripple [5]–[7]. These research studies indicate that the double-line-frequency current ripple has little influence in terms of capacity, cell balancing, temperature rise, and round-trip efficiency. In this case, it is unnecessary to suppress the double-line-frequency current ripple, which will greatly reduce the size of dc-link capacitors. Hence, more competitive cost, higher efficiency, and higher power density can be achieved with single-stage dc–ac converters, which have drawn increasing attention in recent years.

Although an increasing effort has been made on the study of single-stage dc–ac solutions over the years, the single-stage

Manuscript received January 16, 2020; revised April 15, 2020; accepted May 24, 2020. Date of publication May 27, 2020; date of current version September 4, 2020. This work was supported in part by the National Natural Science Foundation of China under Grant 51677085, in part by the Fok Ying-Tong Education Foundation, China, under Grant 161054, and in part by the Fundamental Research Funds for the Central Universities under Grant NE2018102. Recommended for publication by Associate Editor H. S. Krishnamoorthy. *(Corresponding author: Hongfei Wu.)*

The authors are with the College of Automation Engineering, Nanjing University of Aeronautics and Astronautics, Nanjing 211106, China (e-mail: wuhongfei@nuaa.edu.cn; tangxxi@nuaa.edu.cn; zhaojian2017@nuaa.edu.cn; xingyan@nuaa.edu.cn).

Color versions of one or more of the figures in this article are available online at https://ieeexplore.ieee.org.

Digital Object Identifier 10.1109/TPEL.2020.2997981

dc–ac converters still face many challenges: 1) wide operating voltage range not only on the battery side but also on the grid side; 2) isolated bidirectional conversion; and 3) changing the direction of the transferred power quickly. Particularly, the grid voltage changes from zero to hundreds of volts. A buck-type or boost-type converter is not suitable for bidirectional dc–ac power conversion because of the limited voltage conversion range. Hence, the bidirectional single-stage dc–ac converter is still an emergent research topic.

A bidirectional single-stage inverter has been proposed based on the bidirectional flyback converter in [8]. However, disadvantages of the flyback converter, i.e., hard switching, high voltage, and current stresses, make it not a good candidate for high-efficiency power conversion. By integrating a high-frequency transformer, a series of buck-type bidirectional inverters are derived from conventional nonisolated H-bridge inverters [9]–[11]. However, these topologies suffer from large voltage spikes and low efficiency induced by the leakage inductance of the transformer. In [12] and [13], a voltage-clamped circuit has been employed to recycle the energy stored in the leakage inductance. However, too many auxiliary components result in reduced power density. Another solution is based on the well-known dual-active-bridge (DAB) converter [14], [15]. The control algorithm of DAB-based inverters is too complicated owing to nonlinear voltage gain characteristics. In [16] and [17], efforts have been made to achieve zero-voltage switching (ZVS) over the entire range and optimize the efficiency. However, the control system relies on a predetermined lookup table, which makes the system sensitive to parameters of the converter. Qiu *et al.* [18] aim at exploring the possibility of an *LLC* converter in single-stage ac–dc applications. However, a wide operating range results in a small magnetizing inductance and a large circulating current, which will affect the efficiency of the *LLC* converter. Moreover, since the voltage gain cannot be regulated to zero, the zero-crossing distortion is another critical issue. Phase-shift-controlled *LLC* is employed for dc–ac applications in [19] and [20]. The performance is similar to that of the DAB-based solutions.

In [21], a bidirectional resonant converter with voltage-in-phase pulsewidth modulation (VIP-PWM) has been proposed. With VIP-PWM, the voltage gain can be regulated from zero to infinity, which makes it possible to be applied in a single-stage isolated dc–ac converter. Based on the basic principle of the VIP-PWM-controlled resonant converter, a solution for a single-stage isolated bidirectional microinverter is proposed in this article. The major advantages of the proposed solution are as follows.

1) The voltage gain can be theoretically regulated from zero to infinity, which helps avoid the zero-crossing issue of the isolated single-stage dc–ac converter based on the *LLC* converters.
2) The voltage gain is only determined by the duty cycle and is independent of the transferred power.
3) The amplitude and direction of the transferred power can be changed quickly.

A unified current controller can be employed, which is much simpler than single-stage dc–ac solutions based on the bidirectional resonant and DAB converters. In addition, soft switching can also be achieved during most of the grid period.

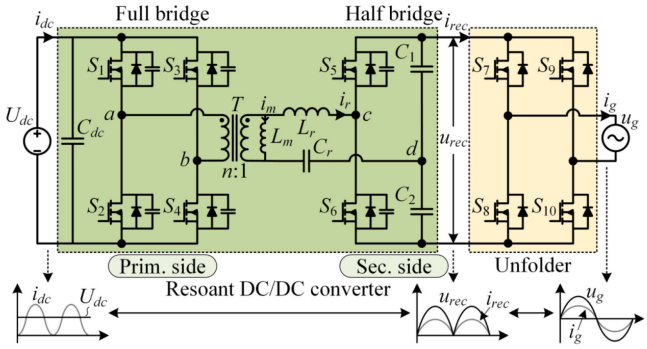

Fig. 2. Proposed bidirectional microinverter.

The rest of this article is organized as follows. The basic idea of VIP-PWM and the detailed operation principle of the proposed microinverter are discussed in Section II. In Section III, characteristics, design considerations, and the corresponding control strategy of the proposed solution are presented. In Section IV, experimental results are provided to verify the performance of the proposed solution. Finally, Section V concludes this article.

II. Proposed Bidirectional Microinverter and Operation Principles

A. Proposed Bidirectional Microinverter

Fig. 2 illustrates the proposed single-stage isolated bidirectional converter. It is composed of two parts: a resonant dc–dc converter and a line-frequency unfolding inverter (unfolder). The resonant converter consists of a full bridge in the primary side and a half bridge in the secondary side, connected by a high-frequency transformer T, a resonant inductor L_r, and a resonant capacitor C_r. Since the dc voltage is relatively low and a higher voltage conversion ratio is required for the bidirectional dc–ac converter, a half bridge is employed in the secondary side of the converter to reduce the turns ratio of the high-frequency transformer. The main purpose of the resonant converter is to regulate the output current and achieve power factor correction (PFC), while the unfolder is employed to reconstruct the pseudo-dc-link current to sinusoidal ac. Both the resonant converter and the unfolder support bidirectional power flow.

B. Basic Idea of VIP-PWM

For *LLC* converters, the voltage conversion ratio is independent of the load only when it operates at the resonant frequency. Inspired by this characteristic, the proposed converter always operates at the resonant frequency, which is expressed as

$$f_r = \frac{1}{2\pi\sqrt{L_r C_r}}. \tag{1}$$

The state function of the resonant current i_r and the voltage u_{Cr} across the resonant capacitor can be expressed as

$$\begin{cases} L_r \frac{di_r}{dt} = u_{ab} - u_{cd} - u_{Cr} \\ C_r \frac{du_{Cr}}{dt} = i_r \end{cases} \tag{2}$$

where u_{ab} and u_{cd} are the midpoint voltages of primary and secondary sides, respectively.

Considering the fundamental component of i_r and u_{Cr}, the state function (2) can be simplified and written as

$$U_{ab1} - U_{cd1} = j\omega_s L_r I_{r1} + \frac{I_{r1}}{j\omega_s C_r} \tag{3}$$

where ω_s is the angular switching frequency, and U_{ab1} and U_{cd1} are the fundamental components of u_{ab} and u_{cd}, respectively.

When the converter operates at the resonant frequency, the fundamental impedance of the resonant tank is equal to zero. In this case, $U_{ab1} = U_{cd1}$, which means that U_{ab1} and U_{cd1} have not only the same amplitude but also the same phase. Accordingly, the midpoint voltages u_{ab} and u_{cd} of primary and secondary sides also share the same phase.

C. Operation Principles of the VIP-PWM Strategy

The normalized voltage conversion ratio is expressed as

$$M_n = \frac{n u_{\rm rec}}{2U_{\rm dc}} \tag{4}$$

where n is the turns ratio of the transformer. According to the voltage conversion ratio, the proposed converter is divided into two modes: buck and boost. The converter operates in the buck mode when $M_n \le 1$, while it operates in the boost mode when $M_n > 1$.

The operation mode of the proposed converter can also be divided into forward and backward modes according to the direction of power flow. In the forward mode, the energy stored in the batteries is transferred to the grid. The proposed converter operates as an inverter. In the backward mode, the converter draws energy from the grid and transmits it to the dc side. The proposed converter operates as a rectifier.

1) Boost Mode: In the boost mode, the duty cycle of the primary-side switches is fixed at 0.5. The output current is regulated by the duty cycle of the secondary-side switches. Fig. 3 illustrates the typical waveforms of the boost mode. Switches in the same leg are driven complementarily. The gating signals of S_1, S_4, and S_5 are in phase. The gating signals of S_2, S_3, and S_6 are in phase as well. In order to ensure symmetrical drive of S_5 and S_6, the switching sequence is S_6–S_5–S_6 in the positive half switching period, and $t_2 - t_1 = t_6 - t_5$. The drive in the negative half switching period is symmetrical to that in the positive half switching period. Since the operation principles of the forward and backward modes are similar, only the forward mode is discussed in detail.

Fig. 3(a) illustrates the typical waveforms in the forward and boost modes. Each switching period can be divided into 12 stages. The equivalent circuits of these stages are shown in Fig. 4.

Stage I $[t_0$–$t_1]$ *[see Fig. 4(a)]:* Before t_0, S_2, S_3, and S_5 are ON, the midpoint voltage u_{ab} of the primary-side bridge is clamped to $-U_{\rm dc}$, while the voltage u_{cd} is clamped to $u_{\rm rec}/2$.

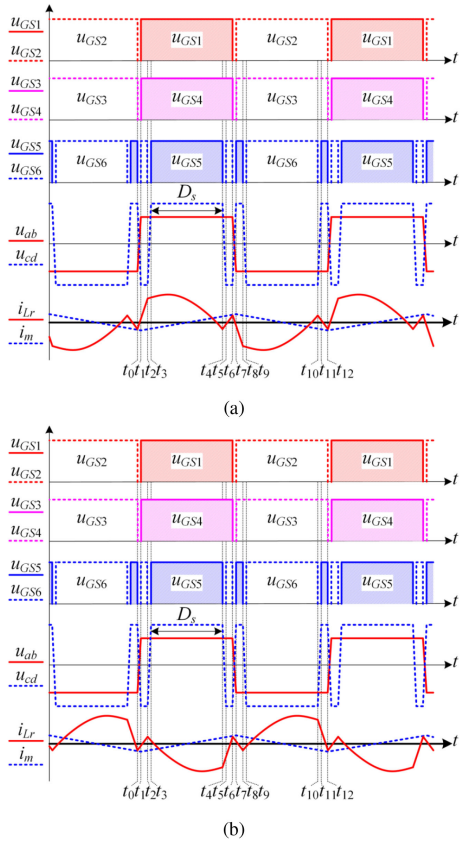

Fig. 3. Typical operating waveforms of the resonant dc–dc converter in the boost mode. (a) Forward mode. (b) Backward mode.

The resonant current i_r and the magnetizing current i_m are negative. At t_0, switches S_2, S_3, and S_5 are turned OFF. Owing to the negative current, the parasitic capacitors of S_2, S_3, and S_5 are charged, while those of S_1, S_4, and S_6 are discharged. Until u_{ab} reaches $U_{\rm dc}$, the parasitic diodes of S_1, S_4, and S_6 are forced to be conducted, and ZVS can be achieved.

Stage II $[t_1$–$t_2]$ *[see Fig. 4(b)]:* At t_1, switches S_1, S_2, and S_6 are turned ON with ZVS. u_{ab} is clamped to $U_{\rm dc}$, while u_{cd} is clamped to $-u_{\rm rec}/2$. The resonant current i_r increases quickly because of a large positive voltage $U_{\rm dc}/n + u_{\rm rec}/2$ applied on the resonant tank. The magnetizing current i_m also increases linearly.

During Stages I and II, u_{cd} is clamped to $-u_{\rm rec}/2$. Therefore, the input voltage charges the resonant tank quickly. The resonant current i_r and the voltage u_{Cr} across the resonant capacitor C_r can be calculated as follows:

$$\begin{aligned} i_r(t) = {} & i_r(t_0)\cos\omega_r(t-t_0) \\ & + \frac{\frac{U_{\rm dc}}{n} + \frac{u_{\rm rec}}{2} - u_{Cr}(t_0)}{Z_r}\sin\omega_r(t-t_0) \end{aligned} \tag{5}$$

$$\begin{aligned} u_{Cr}(t) = {} & i_r(t_0)Z_r\sin\omega_r(t-t_0) + \frac{U_{\rm dc}}{n} + \frac{u_{\rm rec}}{2} \\ & - \left(\frac{U_{\rm dc}}{n} + \frac{u_{\rm rec}}{2} - u_{Cr}(t_0)\right)\cos\omega_r(t-t_0) \end{aligned} \tag{6}$$

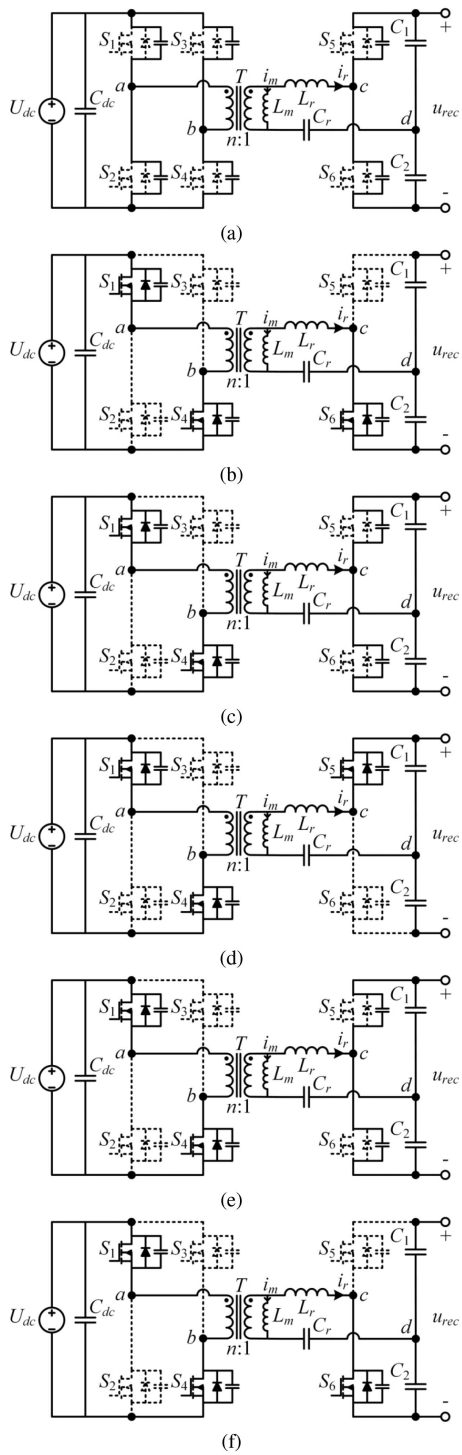

Fig. 4. Equivalent circuits of the resonant dc–dc converter in the boost mode. (a) $[t_0$–$t_1]$. (b) $[t_1$–$t_2]$. (c) $[t_2$–$t_3]$. (d) $[t_3$–$t_4]$. (e) $[t_4$–$t_5]$. (f) $[t_5$–$t_6]$.

where $\omega_r = 2\pi f_r$ is the angular frequency and $Z_r = \sqrt{L_r/C_r}$ is the characteristic impedance of the series-resonant tank.

Stage III $[t_2$–$t_3]$ *[see Fig. 4(c)]:* At t_2, S_6 is turned OFF. The parasitic capacitor of S_6 is charged by the positive resonant current, and the parasitic capacitor of S_5 is discharged. Since the resonant current is relatively large, S_5 can easily achieve ZVS.

Stage IV $[t_3$–$t_4]$ *[see Fig. 4(d)]:* At t_3, S_5 is turned ON with ZVS. u_{cd} is clamped to $u_{\rm rec}/2$. The resonant inductor L_r resonates with the resonant capacitor C_r. i_m keeps increasing linearly owing to the positive voltage u_{ab} clamped to $U_{\rm dc}$.

During the two stages, L_r resonates with C_r. Most of the power is transferred during these two stages. i_r and u_{Cr} can be expressed as

$$i_r(t) = i_r(t_2)\cos\omega_r(t-t_2) + \frac{\frac{U_{\rm dc}}{n} - \frac{u_{\rm rec}}{2} - u_{Cr}(t_2)}{Z_r}\sin\omega_r(t-t_2) \tag{7}$$

$$u_{Cr}(t) = i_r(t_2)Z_r\sin\omega_r(t-t_2) + \frac{U_{\rm dc}}{n} - \frac{u_{\rm rec}}{2} - \left(\frac{U_{\rm dc}}{n} - \frac{u_{\rm rec}}{2} - u_{Cr}(t_2)\right)\cos\omega_r(t-t_2). \tag{8}$$

Stage V $[t_4$–$t_5]$ *[see Fig. 4(e)]:* At t_4, S_5 is turned OFF. The negative resonant current charges the parasitic capacitor of S_5 and discharges the parasitic capacitor of S_6. Until u_{cd} is reduced to $-u_{\rm rec}/2$, the body diode of S_6 is conducted, and ZVS can be achieved at light load. However, the resonant current is reduced and close to zero at heavy load. It is difficult for S_6 to achieve ZVS at t_5. However, fortunately, zero-current switching (ZCS) of S_6 can still be achieved.

Stage VI $[t_5$–$t_6]$ *[see Fig. 4(f)]:* At t_5, S_6 is turned ON with ZCS. The resonant current increases owing to a positive voltage applied on the series-resonant tank.

During Stages V and VI, u_{cd} is clamped to $-u_{\rm rec}/2$. i_r and u_{Cr} can be calculated as follows:

$$i_r(t) = i_r(t_4)\cos\omega_r(t-t_4) + \frac{\frac{U_{\rm dc}}{n} + \frac{u_{\rm rec}}{2} - u_{Cr}(t_4)}{Z_r}\sin\omega_r(t-t_4) \tag{9}$$

$$u_{Cr}(t) = i_r(t_4)Z_r\sin\omega_r(t-t_4) + \frac{U_{\rm dc}}{n} + \frac{u_{\rm rec}}{2} - \left(\frac{U_{\rm dc}}{n} + \frac{u_{\rm rec}}{2} - u_{Cr}(t_4)\right)\cos\omega_r(t-t_4). \tag{10}$$

The operation principles of the rest of the stages are symmetrical to the positive half switching period and hence will not be discussed again.

2) Buck Mode: In the buck mode, the switches in the secondary side always operate with a duty cycle of 0.5, while the duty cycle of switches in the primary side is modulated to regulate the output. Fig. 5 shows typical waveforms of the buck mode. The operation principle of the buck mode is similar to that of the boost mode and will not be presented in this article.

III. Characteristics and Design Considerations

A. Voltage Conversion Ratio Characteristics

1) Boost Mode: In the boost mode, the duty cycle D_p is fixed at 0.5, while the duty cycle D_s is employed to regulate the grid current. According to the waveforms in Fig. 3, t_0, t_2, t_4, and t_6

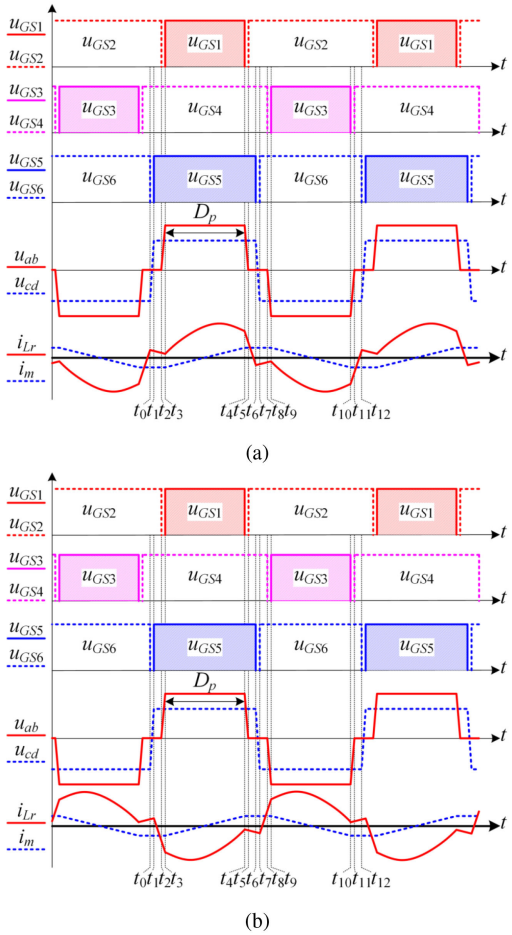

Fig. 5. Typical operating waveforms of the resonant dc–dc converter in the buck mode. (a) Forward mode. (b) Backward mode.

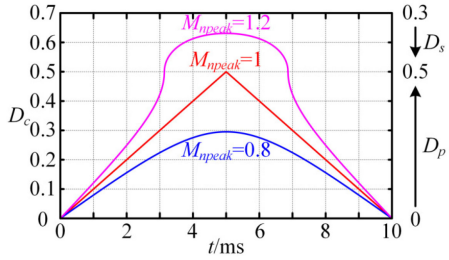

Fig. 6. Ideal duty cycle during half grid period.

can be expressed by the duty cycle D_s, as follows:

$$\begin{cases} t_0 = 0 \\ t_2 = \frac{1-2D_s}{4}T_s \\ t_4 = \frac{1+2D_s}{4}T_s \\ t_6 = \frac{T_s}{2} \end{cases} \tag{11}$$

where $T_s = 1/f_s$ is the switching period.

Substituting (11) into (5)–(10), the resonant current i_r and the resonant voltage u_{Cr} at t_2, t_4, and t_6 can be derived, respectively, as follows:

$$\begin{cases} i_r(t_2) = i_r(t_0)\sin(\pi D_s) \\ \qquad + \dfrac{\frac{U_{\rm dc}}{n} + \frac{u_{\rm rec}}{2} - u_{Cr}(t_0)}{Z_r}\cos(\pi D_s) \\ u_{Cr}(t_2) = i_r(t_0)Z_r\cos(\pi D_s) + \dfrac{U_{\rm dc}}{n} + \dfrac{u_{\rm rec}}{2} \\ \qquad - (\dfrac{U_{\rm dc}}{n} + \dfrac{u_{\rm rec}}{2} - u_{Cr}(t_0))\sin(\pi D_s) \end{cases} \tag{12}$$

$$\begin{cases} i_r(t_4) = -i_r(t_0)\sin(\pi D_s) \\ \qquad + \dfrac{\frac{U_{\rm dc}}{n} - u_{Cr}(t_0)}{Z_r}\cos(\pi D_s) \\ \qquad + \dfrac{u_{\rm rec}}{2Z_r}(\cos\pi D_s - 2\sin 2\pi D_s) \\ u_{Cr}(t_4) = i_r(t_0)Z_r\cos(\pi D_s) + \dfrac{U_{\rm dc}}{n} - \dfrac{u_{\rm rec}}{2} \\ \qquad + \dfrac{\frac{U_{\rm dc}}{n} - u_{Cr}(t_0)}{Z_r}\sin(\pi D_s) \\ \qquad + \dfrac{u_{\rm rec}}{2}(\sin\pi D_s + 2\cos 2\pi D_s) \end{cases} \tag{13}$$

$$\begin{cases} i_r(t_6) = -i_r(t_0) \\ u_{Cr}(t_6) = -u_{Cr}(t_0) + \dfrac{2U_{\rm dc}}{n} \\ \qquad + \dfrac{u_{\rm rec}}{2}(2 - 4\sin\pi D_s). \end{cases} \tag{14}$$

Owing to the symmetrical operations of the resonant dc–dc converter, the resonant voltage u_{C_r} at t_6 satisfies

$$u_{C_r}(t_6) = -u_{C_r}(t_0). \tag{15}$$

Using (14) and (15), the normalized voltage conversion ratio in the boost mode can be derived and expressed as

$$M_{\rm Boost} = \frac{nu_{\rm rec}}{2U_{\rm dc}} = \frac{1}{2\sin(\pi D_s) - 1}. \tag{16}$$

The above analysis is performed for the forward mode. The derived normalized voltage conversion ratio is only determined by the duty cycle D_s and is independent of the amplitude and the direction of the transferred power. Therefore, it is believed that (16) is still valid for the backward mode.

2) Buck Mode: In the buck mode, D_s is fixed at 0.5, and D_p is employed to regulate the power flow. Similarly, the normalized voltage conversion ratio can be derived as

$$M_{\rm Buck} = \frac{nu_{\rm rec}}{2U_{\rm dc}} = \sin(\pi D_p). \tag{17}$$

Actually, the normalized voltage conversion ratio can be written as a uniform expression, as follows:

$$M_n = \frac{nu_{\rm rec}}{2U_{\rm dc}} = \frac{\sin(\pi D_p)}{2\sin(\pi D_s) - 1}. \tag{18}$$

As aforementioned, the output voltage of the resonant dc–dc converter is rectified sinusoidally. Thus, the ideal duty cycle for the dc–ac operation can be obtained, as shown in Fig. 6, where $M_{n\rm peak}$ is the peak value of the normalized voltage conversion ratio, i.e., $\frac{nU_g}{2U_{\rm dc}}$.

B. ZVS Analysis

According to the operation principles in Section II-C, when the converter operates in the buck mode, ZVS of S_1 and S_3 is difficult to achieve in the forward mode, while ZVS of S_2 and S_4 is difficult to achieve in the backward mode. Fortunately, ZVS of the primary-side switches can be achieved with the help of the magnetizing inductance L_m. On the contrary, ZVS of the secondary-side switches is much easier to achieve, since the phase of resonant current is in advance.

Owing to the symmetry, the ZVS constraint condition for S_1 and S_3 is the same as that of S_2 and S_4. Therefore, only the ZVS of S_1 is taken as an example to be discussed here. To achieve ZVS for S_1, the resonant current i_r and the magnetizing current i_m must satisfy

$$i_r(t_2) + i_m(t_2) < \frac{nC_pU_{\rm dc}}{T_d} \tag{19}$$

where C_p is the total parasitic capacitance of switches and T_d is the dead time. $i_m(t_2)$ is the value of i_m at t_2, expressed by (20). Substituting (20) into (19), the magnetizing inductance L_m should satisfy (21)

$$i_m(t_2) = -\frac{nD_pU_{\rm dc}}{2f_rL_m} \tag{20}$$

$$L_m < \frac{nD_pU_{\rm dc}}{2f_r(i_r(t_2) - \frac{nC_pU_{\rm dc}}{T_d})}. \tag{21}$$

To calculate the value of the resonant current, the analysis is conducted in the frequency domain. With the Fourier transform, the mth-order harmonic components of u_{ab} and u_{cd} are derived as follows:

$$U_{abm} = \begin{cases} \frac{4U_{\rm dc}}{m\pi}\sin(m\pi D_p)e^{\frac{\pi}{2}i} & m = 1,5,9\ldots \\ -\frac{4U_{\rm dc}}{m\pi}\sin(m\pi D_p)e^{\frac{\pi}{2}i} & m = 3,7,11\ldots \end{cases} \tag{22}$$

$$U_{cdm} = \begin{cases} \frac{2u_{\rm rec}}{m\pi}(2\sin(m\pi D_s) - 1)e^{\frac{\pi}{2}i} & m = 1,5,9\ldots \\ \frac{2u_{\rm rec}}{m\pi}(-2\sin(m\pi D_s) - 1)e^{\frac{\pi}{2}i} & m = 3,7,11\ldots. \end{cases} \tag{23}$$

Accordingly, the mth-order harmonic components of i_r are expressed in (24). It should be noted that the harmonic components of i_r only generate reactive current and do not participate in the transmission of active power

$$I_{rm} = \frac{U'_{abm} - U_{cdm}}{(jm + 1/jm)Z_r}, \quad m = 3,5,7\ldots \tag{24}$$

where $U'_{abm} = U_{abm}/n$ is the mth-order harmonics of u_{ab} reflected to the secondary side.

In contrast, the impedance of the resonant tank at the resonant frequency is equal to zero. Considering the influence of parasitic resistance of switches, the fundamental component of resonant current I_{r1} is in phase with u_{ab} and u_{cd}, expressed by (25). Since the power is only transferred by the fundamental component with the VIP-PWM, the instantaneous output power can be expressed by (26), as follows:

$$I_{r1} = I_{r1m}e^{\frac{\pi}{2}i} \tag{25}$$

$$p_g = 2f_r\int_{t_0}^{t_6}\frac{u_{\rm rec}}{2}i_{r1}dt \tag{26}$$

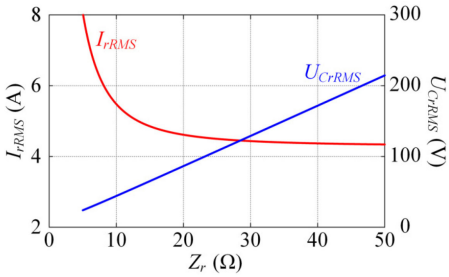

Fig. 7. Current stress and voltage stress of the resonant tank when $U_{\rm dc} = 40$ V, $u_{\rm rec} = 310$ V, and $p_g = 600$ W.

where I_{r1m} is the amplitude of the fundamental component of the resonant current, p_g is the instantaneous value of the grid power, and $i_{r1} = I_{r1m}\sin(\omega_r t)$ is the fundamental component of the resonant current in the time domain. Accordingly, I_{r1} can be simplified and expressed by (27). Then, $i_r(t_2)$ can be calculated by (28) with a numerical method, as follows:

$$I_{r1} = \frac{\pi i'_{\rm rec}}{2\sin(\pi D_s) - 1}e^{\frac{\pi}{2}i} \tag{27}$$

$$i_r(t_2) = \sum_{m=1}^{\infty} i_{rm}(t_2) \tag{28}$$

where $i_{rm}(t_2)$ is the value of the mth-order harmonic current at t_2.

When the resonant dc–dc converter operates in the boost mode, ZVS of the primary-side switches can be achieved easily because of the lag of resonant current. ZVS of the secondary-side switches is difficult to achieve at some switching moment, but ZCS can be achieved easily.

For dc–ac power conversion, the voltage gain needs to be regulated to zero. It is difficult and unnecessary to achieve ZVS during the entire operating range. Otherwise, the magnetizing inductance would be designed to be a very low value, resulting in large circulating losses. To optimize the efficiency, ZVS needs to be achieved only during the time when most of the power is transferred. In this article, ZVS of primary-side switches is designed to be achieved when $u_{\rm rec} > 250$ V. During this interval, 70% of the grid power is being transferred.

C. Design Consideration of the Resonant Tank

The major design consideration of the resonant tank is to decrease circulating current and improve efficiency. As seen from (24), the harmonics of the resonant current decrease with the increasing of Z_r. Fig. 7 shows the curve of the rms value of the resonant current $I_{r\rm RMS}$ versus Z_r. Therefore, Z_r should be designed as large as possible to decrease conduction losses caused by the circulating current. However, the size of L_r would also increase with the increase in L_r, resulting in larger losses of the resonant inductor. In addition, the larger the Z_r, the larger the voltage ripples across the resonant capacitor. The voltage ripples across the resonant capacitor should not be too large. In practice, L_r is selected at the inflection point of the curve of $I_{r\rm RMS}$ versus L_r.

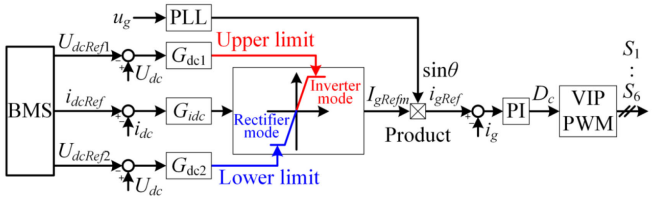

Fig. 8. Control block of the proposed solution.

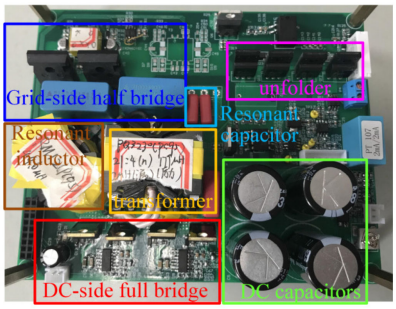

Fig. 9. Experimental prototype of the proposed microinverter.

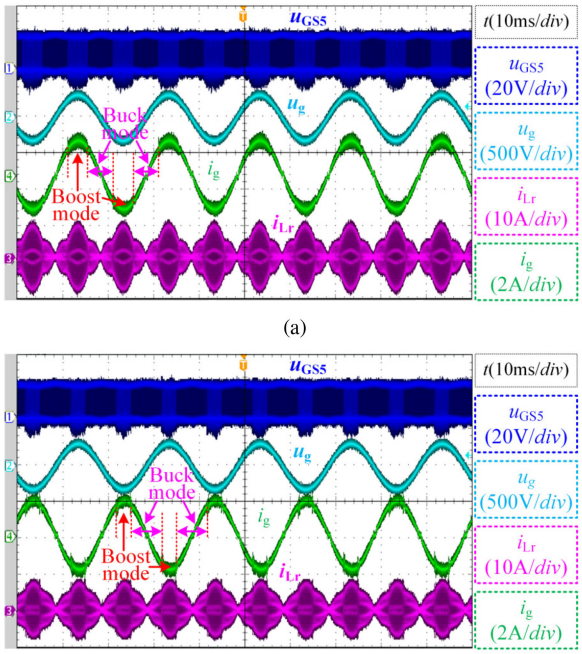

Fig. 10. Steady-state waveforms of the proposed solution at an input voltage of 25 V and an output power of 300 W. (a) Inverter. (b) Rectifier.

D. Control Strategy

According to the analysis in Section III-A, the voltage conversion ratio is only determined by the duty cycle and is independent of the value and the direction of the transferred power. The same modulation strategy is adopted for both forward and backward modes. Therefore, a unified controller can be used to regulate the output power in both inverter and rectification modes.

The control block of the proposed solution is illustrated in Fig. 8. A battery management system is employed to generate the reference dc current $i_{\rm dcRef}$ and manage the charging/discharging progress of the battery. When $i_{\rm dcRef} > 0$, the proposed microinverter operates in the inverter mode. When $i_{\rm dcRef} < 0$, the proposed microinverter operates in the rectification mode. The output of the dc current controller is used as the amplitude of the reference grid current $I_{g{\rm Ref}m}$. In order to prevent the battery from overcharging and overdischarging, two additional dc voltage controllers are employed. The controller $G_{\rm dc1}$ generates the upper limit of the grid current and prevents overdischarging of the battery, while the discharging voltage is limited to $U_{\rm dcRef2}$ by the controller $G_{\rm dc2}$ to prevent the battery from overcharging. To achieve unit power factor, a phase-locked loop is employed to track the frequency and phase of the grid voltage. Then, the reference grid current is expressed by

$$i_{g{\rm Ref}} = I_{g{\rm Ref}m} \sin\theta \tag{29}$$

where θ is the phase of the grid voltage. With the inner grid current controller, the grid current can track the grid voltage and achieve PFC control.

IV. Experimental Verification

A 300-W experimental prototype, as shown in Fig. 9, is established to verify the effectiveness of the proposed solution. The dc side, whose voltage is 25–40 V, is connected to a bidirectional power supply. The ac side is connected to a 220-Vrms ac grid, provided by an ac power source. The switching frequency of the converter is 100 kHz. The detailed parameters are listed as follows: $n = 4/21$, $L_r = 46.1\ \mu$H, $C_r = 55$ nF, $L_m = 180\ \mu$H, S_1–S_4 IRFB3307ZPbF, S_5 and S_6 SCT3080AL, S_7–S_{10} FDPF20N50, $C_1 = C_2 = 2.2\ \mu$F, and dc-side filter capacitor $C_{\rm dc} = 7.2$ mF.

Fig. 10 illustrates the steady-state waveforms of the converter with an input voltage of 25 V and an output power of 300 W. Since the input dc voltage is relatively small, both buck and boost modes are employed to control the output current. The boundary of buck and boost modes in the inverter mode is $|u_g| = 270$ V. In the rectification mode, mode transition happens when $|u_g| = 280$ V. Owing to the parasitic resistance, the voltage conversion ratio in the rectification mode is slightly larger than that in the inverter mode, which results in the difference of the boundary of mode transition.

As aforementioned, the worst case for ZVS achievement is at full load. Therefore, ZVS performance has been tested at 25-V input voltage and full load in the inverter mode. It is found that S_2 can achieve ZVS during almost whole grid period, while the ZVS of S_1 can be achieved when the grid voltage is greater than 170 V with 25-V dc input voltage, as shown in Fig. 11.

In the buck mode, the resonant current i_r lags u_{cd}. Therefore, it is easy for the switches in the secondary side to achieve ZVS. In the boost mode, S_5 turns ON three times in each switching period, i.e., t_a, t_b, and t_c. As shown in Fig. 12, ZVS is achieved at t_a and t_b, but lost at t_c. Fortunately, the value of the resonant current at t_c is approximately equal to zero, which means that S_5 can still operate with ZCS.

In order to verify the dynamic performance of the proposed solution, mode transition between the inverter mode and the rectification mode is tested at the peak voltage point of the grid

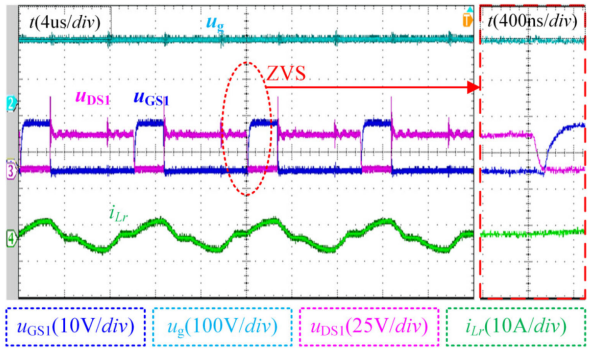

Fig. 11. ZVS performance of S_1 at full load in the inverter mode when $U_{dc} = 25$ V and $u_{rec} = 170$ V.

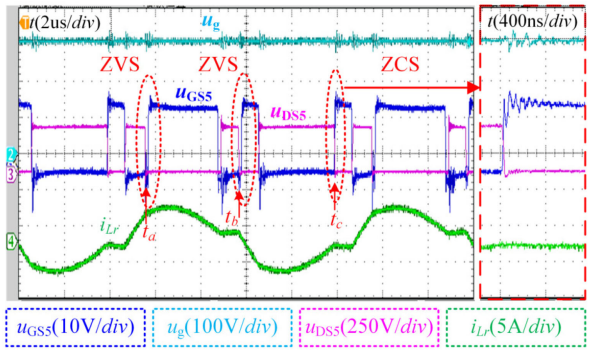

Fig. 12. ZVS performance of S_5 at full load in the inverter mode when $U_{dc} = 25$ V and $u_{rec} = 310$ V.

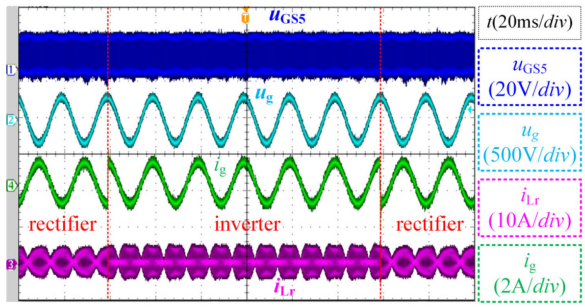

Fig. 13. Dynamic performance during load stepping at an input voltage of 35 V.

voltage. The experimental results are illustrated in Fig. 13. It is seen that the operation mode can be quickly switched between the inverter mode and the rectification mode.

The efficiency is measured at different circumstances, as shown in Fig. 14. When the transferred power is higher than zero, the proposed converter operates as an inverter, otherwise as a rectifier. The efficiency at full load is higher than 92% for both inverter and rectification modes. A peak efficiency of 96.9% is obtained at an input voltage of 30 V and an output power of 120 W in the rectification mode.

The total harmonic distortion (THD) of the grid current is tested when the converter operates as an inverter and a rectifier, as shown in Fig. 15. The THD of the grid current decreases with the increase in the transferred power. It is seen that the THD is

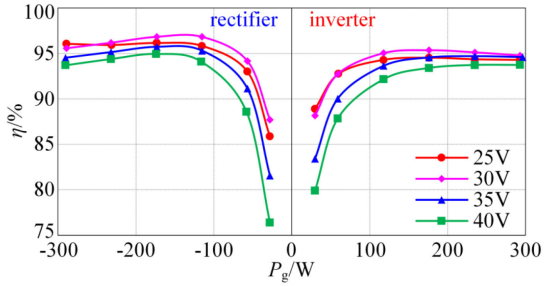

Fig. 14. Measured efficiency of the proposed solution.

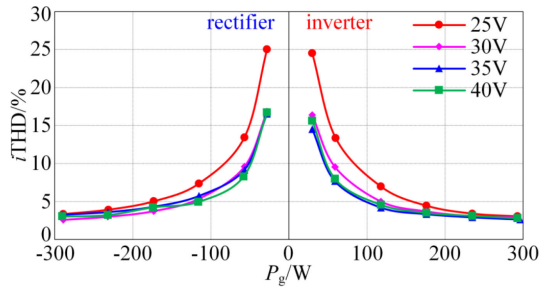

Fig. 15. Measured THD of the grid current.

TABLE I
FEATURES AND PERFORMANCE OF THE PROPOSED SOLUTION AND PREVIOUS WORK

Parameters	Proposed solution	DAB-based solution [16]
DC voltage	25V-40V	370V-470V
Grid voltage	220V	230V
Grid frequency	50Hz	50Hz
Output power	300W	3.7kW
Switching frequency	100kHz	75kHz-120kHz
Peak efficiency	96.9%	96.3%
Current THD at full load	2.6%-3.3%	3.2%-3.9%

less than 5% when the output power is greater than 50% rated power, no matter whether the converter operates in the inverter mode or the rectification mode. When the presented converter operates as a rectifier with an input voltage of 30 V and an output power of 300 W, the minimum THD of 2.6% is achieved.

A brief comparison with the DAB-based bidirectional microinverter in [16] is conducted, as shown in Table I. It is seen that both the efficiency and the THD performance of the proposed solution for a 300-W output are better than those of the DAB-based 3.7-kW bidirectional ac–dc converter.

V. CONCLUSION

In this article, a single-stage single-phase isolated bidirectional microinverter based on the VIP-PWM-controlled resonant converter was proposed and investigated for energy storage applications. With the VIP-PWM control, the voltage conversion ratio of the resonant converter was able to vary in a wide range, and step-up and step-down voltage conversion was achieved. The amplitude and the direction of the transferred power can be changed quickly and smoothly with a simple unified current controller. Soft switching was also achieved during most of the grid period. A 300-W prototype with an input voltage of

25–40 V and a grid voltage of 220 Vac was established to verify the effectiveness and feasibility of the proposed converter. Experimental results demonstrated the analysis performed in this article. The proposed microinverter achieved a peak efficiency of 96.9% and a minimum THD of 2.6%.

REFERENCES

[1] B. K. Bose, "Global energy scenario and impact of power electronics in 21st century," *IEEE Trans. Power Electron.*, vol. 60, no. 7, pp. 2638–2651, Jul. 2013.

[2] L. Zhang, K. Sun, Y. W. Li, X. Lu, and J. Zhao, "A distributed power control of series-connected module integrated inverters for PV grid-tied applications," *IEEE Trans. Power Electron.*, vol. 33, no. 9, pp. 7698–7707, Sep. 2018.

[3] H. B. Hu, S. Harb, N. Kutkut, I. Batarseh, and Z. J. Shen, "A review of power decoupling techniques for microinverters with three different decoupling capacitor locations in PV systems," *IEEE Trans. Power Electron.*, vol. 28, no. 6, pp. 2711–2726, Jun. 2013.

[4] A. Pal and K. Basu, "A unidirectional single-stage three-phase soft-switched isolated DC-AC converter," *IEEE Trans. Power Electron.*, vol. 34, no. 2, pp. 1142–1158, Feb. 2019.

[5] S. Bala, T. Tengnér, P. Rosenfeld, and F. Delince, "The effect of low frequency current ripple on the performance of a Lithium Iron Phosphate (LFP) battery energy storage system," in *Proc. IEEE Energy Convers. Congr. Expo.*, Raleigh, NC, USA, 2012, pp. 3485–3492.

[6] T. H. Kim *et al.*, "Analytical study on low-frequency ripple effect of battery charging," in *Proc. IEEE Veh. Power Propulsion Conf.*, Seoul, South Korea, 2012, pp. 809–811.

[7] H. Z. Z. Beh, G. A. Covic, and J. T. Boys, "Effects of pulse and DC charging on lithium iron phosphate ($LiFePO_4$) batteries," in *Proc. IEEE Energy Convers. Congr. Expo.*, Denver, CO, USA, 2013, pp. 315–320.

[8] Y. S. Jeong, S. H. Lee, S. G. Jeong, J. M. Kwon, and B. H. Kwon, "High-efficiency bidirectional grid-tied converter using single power conversion with high-quality grid current," *IEEE Trans. Ind. Electron.*, vol. 64, no. 11, pp. 8504–8513, Nov. 2017.

[9] P. T. Krein, R. S. Balog, and X. Geng, "High-frequency link inverter for fuel cells based on multiple-carrier PWM," *IEEE Trans. Power Electron.*, vol. 19, no. 5, pp. 1279–1288, Sep. 2004.

[10] J. R. Kan, S. J. Xie, Y. Y. Wu, Y. Tang, Z. L. Yao, and R. Chen, "High-frequency-link inverter using combined synchronous rectifiers," *IEEE Trans. Ind. Electron.*, vol. 61, no. 12, pp. 6769–6777, Dec. 2014.

[11] R. K. Surapaneni, D. B. Yelaverthi, and A. K. Rathore, "Cycloconverter-based double-ended microinverter topologies for solar photovoltaic AC module," *IEEE J. Emerg. Sel. Topics Power Electron.*, vol. 4, no. 4, pp. 1354–1361, Dec. 2016.

[12] W. J. Zhu, K. L. Zhou, and M. Cheng, "A bidirectional high-frequency-link single-phase inverter: Modulation, modeling, and control," *IEEE Trans. Power Electron.*, vol. 29, no. 8, pp. 4049–4057, Aug. 2014.

[13] S. Zhong, J. P. Xu, and X. Zhou, "High-efficiency zero-voltage switching single-stage switching amplifier with half-bridge active clamping circuit," *IEEE Trans. Ind. Electron.*, vol. 65, no. 11, pp. 8574–8584, Nov. 2018.

[14] N. D. Weise, G. Castelino, K. Basu, and N. Mohan, "A single-stage dual-active-bridge-based soft switched AC-DC converter with open-loop power factor correction and other advanced features," *IEEE Trans. Power Electron.*, vol. 29, no. 8, pp. 4007–4016, Aug. 2014.

[15] T. Chen, R. Yu, Q. Huang, and A. Q. Huang, "A single-stage bidirectional dual-active-bridge AC-DC converter based on enhancement mode GaN power transistor," in *Proc. IEEE Appl. Power Electron. Conf. Expo.*, San Antonio, TX, USA, 2018, pp. 723–728.

[16] J. Everts, F. Krismer, J. Van den Keybus, J. Driesen, and J. W. Kolar, "Optimal ZVS modulation of single-phase single-stage bidirectional DAB AC-DC converters," *IEEE Trans. Power Electron.*, vol. 29, no. 8, pp. 3954–3970, Aug. 2014.

[17] F. Jauch and J. Biela, "Combined phase-shift and frequency modulation of a dual-active-bridge AC-DC converter with PFC," *IEEE Trans. Power Electron.*, vol. 31, no. 12, pp. 8387–8397, Dec. 2016.

[18] Y. Qiu, W. Liu, P. Fang, Y. Liu, and P. C. Sen, "A mathematical guideline for designing an AC-DC LLC converter with PFC," in *Proc. IEEE Appl. Power Electron. Conf. Expo.*, San Antonio, TX, USA, 2018, pp. 2001–2008.

[19] D. S. y. Rosas, D. Frey, J. Schanen, and J. Ferrieux, "Close loop control to bidirectional isolated single stage DAB with resonant circuit DC/AC converter to connection of batteries to the single phase grid," in *Proc. IEEE Appl. Power Electron. Conf. Expo.*, Tampa, FL, USA, 2017, pp. 1333–1340.

[20] D. R. Nayanasiri, D. M. Vilathgamuwa, and D. L. Maskell, "Half-wave cycloconverter-based photovoltaic microinverter topology with phase-shift power modulation," *IEEE Trans. Power Electron.*, vol. 28, no. 6, pp. 2700–2710, Jun. 2013.

[21] H. Wu, S. Ding, K. Sun, L. Zhang, Y. Li, and Y. Xing, "Bidirectional soft-switching series-resonant converter with simple PWM control and load-independent voltage-gain characteristics for energy storage system in DC microgrids," *IEEE J. Emerg. Sel. Topics Power Electron.*, vol. 5, no. 3, pp. 995–1007, Sep. 2017.

Hongfei Wu (Senior Member, IEEE) received the B.S. and Ph.D. degrees in electrical engineering and power electronics and power drives from the Nanjing University of Aeronautics and Astronautics (NUAA), Nanjing, China, in 2008 and 2013, respectively.

Since 2013, he has been with the Faculty of Electrical Engineering, NUAA, where he is currently a Professor with the College of Automation Engineering. He has authored or coauthored more than 170 peer-reviewed papers published in journals and conference proceedings. He is the holder of more than 30 patents. His research interests include power converters, wide-bandgap device applications, and magnetic integration.

Dr. Wu was the recipient of the awards of the Outstanding Reviewer for the IEEE TRANSACTIONS ON POWER ELECTRONICS in 2013 and the Best Associate Editor for the *Journal of Power Electronics* in 2018. He was a recipient of the Changkong Scholar Award and the Young Scholar Innovation Award of NUAA in 2017. He is an Associate Editor for the *Journal of Power Electronics* and the *CPSS Transactions on Power Electronics and Applications*.

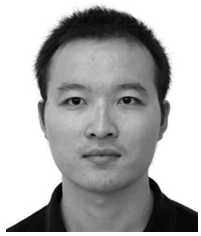

Xinxi Tang was born in Jiangsu, China, in 1992. He received the B.S. degree in electrical engineering in 2014 from the Nanjing University of Aeronautics and Astronautics, Nanjing, China, where he is currently working toward the Ph.D. degree in electrical engineering and power drives.

His research interests include topology and control of ac–dc converters and resonant converters.

Jian Zhao was born in Jiangsu, China, in 1995. He received the B.S. degree in electrical engineering in 2017 from the Nanjing University of Aeronautics and Astronautics, Nanjing, China, where he is currently working toward the master's degree in electrical engineering.

His research interests include topology and control of dc–dc converters.

Yan Xing (Member, IEEE) received the B.S. and M.S. degrees in automation and electrical engineering from Tsinghua University, Beijing, China, in 1985 and 1988, respectively, and the Ph.D. degree in electrical engineering from the Nanjing University of Aeronautics and Astronautics (NUAA), Nanjing, China, in 2000.

Since 1988, she has been with the Faculty of Electrical Engineering, NUAA, where she is currently a Professor with the College of Automation Engineering. She has authored more than 200 technical papers published in journals and conference proceedings and three books. Her research interests include topology and control for dc–dc and dc–ac converters.

Dr. Xing is an Associate Editor for the IEEE TRANSACTIONS ON POWER ELECTRONICS. She is a member of the Committee on Renewable Energy Systems of the IEEE Industrial Electronics Society.